Author/s:
Wang, Y;Arandiyan, H;Mofarah, SS;Shen, X;Bartlett, SA;Koshy, P;Sorrell, CC;Sun, H;Pozo-Gonzalo, C;Dastafkan, K;Britto, S;Bhargava, SK;Zhao, C

Title:
Stacking Fault-Enriched MoNi4/MoO2 Enables High-Performance Hydrogen Evolution

Date:
2024-08-15

Citation:
Wang, Y., Arandiyan, H., Mofarah, S. S., Shen, X., Bartlett, S. A., Koshy, P., Sorrell, C. C., Sun, H., Pozo-Gonzalo, C., Dastafkan, K., Britto, S., Bhargava, S. K. & Zhao, C. (2024). Stacking Fault-Enriched MoNi4/MoO2 Enables High-Performance Hydrogen Evolution. Advanced Materials, 36 (33), https://doi.org/10.1002/adma.202402156.

Persistent Link:
https://hdl.handle.net/11343/351026

ADVANCED MATERIALS
www.advmat.de

Stacking Fault-Enriched $MoNi_4/MoO_2$ Enables High-Performance Hydrogen Evolution

Yuan Wang, Hamidreza Arandiyan,* Sajjad S. Mofarah, Xiangjian Shen, Stuart A. Bartlett, Pramod Koshy, Charles C. Sorrell, Hongyu Sun, Cristina Pozo-Gonzalo, Kamran Dastafkan, Sylvia Britto, Suresh K. Bhargava, and Chuan Zhao**

Producing green hydrogen in a cost-competitive manner via water electrolysis will make the long-held dream of hydrogen economy a reality. Although platinum (Pt)-based catalysts show good performance toward hydrogen evolution reaction (HER), the high cost and scarce abundance challenge their economic viability and sustainability. Here, a non-Pt, high-performance electrocatalyst for HER achieved by engineering high fractions of stacking fault (SF) defects for $MoNi_4/MoO_2$ nanosheets (d-MoNi) through a combined chemical and thermal reduction strategy is shown. The d-MoNi catalyst offers ultralow overpotentials of 78 and 121 mV for HER at current densities of 500 and 1000 mA cm^{-2} in 1 M KOH, respectively. The defect-rich d-MoNi exhibits four times higher turnover frequency than the benchmark 20% Pt/C, together with its excellent durability (> 100 h), making it one of the best-performing non-Pt catalysts for HER. The experimental and theoretical results reveal that the abundant SFs in d-MoNi induce a compressive strain, decreasing the proton adsorption energy and promoting the associated combination of *H into hydrogen and molecular hydrogen desorption, enhancing the HER performance. This work provides a new synthetic route to engineer defective metal and metal alloy electrocatalysts for emerging electrochemical energy conversion and storage applications.

1. Introduction

Green hydrogen produced from electrochemical water splitting powered by renewable energy has drawn extensive attention as a clean-energy carrier for replacing fossil fuels, a key step toward addressing global energy and climate change issues.[1] The current industrial water electrolysis is based on proton exchange membrane (PEM) water electrolysis and alkaline water electrolysis. Unlike PEM, which requires noble metal-based catalysts in acidic media, alkaline electrolyzers expand the choice of catalysts to non-noble metal-based catalysts, making them more sustainable for large-scale hydrogen production.[2] The half reaction-hydrogen evolution reaction (HER) requires efficient and stable electrocatalysts to overcome the sluggish reaction kinetics and harsh operating conditions.[3] Platinum (Pt) is the most efficient HER catalyst, typically exhibiting an onset potential close to the thermodynamic

Y. Wang
Department of Chemical Engineering
The University of Melbourne
Parkville, VIC 3010, Australia
E-mail: helena.wang@unimelb.edu.au

H. Arandiyan
Laboratory of Advanced Catalysis for Sustainability
School of Chemistry
University of Sydney
Sydney, NSW 2006, Australia
E-mail: hamid.arandiyan@sydney.edu.au

The ORCID identification number(s) for the author(s) of this article can be found under https://doi.org/10.1002/adma.202402156

DOI: 10.1002/adma.202402156

H. Arandiyan, S. K. Bhargava
Centre for Applied Materials and Industrial Chemistry (CAMIC)
School of Science
RMIT University
Melbourne, VIC 3001, Australia

S. S. Mofarah, P. Koshy, C. C. Sorrell
School of Materials Science and Engineering
UNSW Sydney
Sydney, NSW 2052, Australia

X. Shen
Engineering Research Centre of Advanced Functional Material Manufacturing of Ministry of Education
Zhengzhou University
Zhengzhou 450001, P. R. China

S. A. Bartlett, S. Britto
Diamond Light Source
Harwell Science and Innovation Campus
Didcot OX11 0DE, UK

H. Sun
School of Resources and Materials
Northeastern University at Qinhuangdao
Qinhuangdao 066004, P. R. China

potential (0 V vs reverse hydrogen electrode, RHE), small Tafel slope, and a high exchange current density. However, the high cost and insufficient reserves of Pt resources have restricted the application at a large scale and constrained the scalable hydrogen generation.[4] Nickel is a low-cost and Earth-abundant alternative to noble metal electrocatalysts.[5] However, the HER performance of the Ni catalysts is sub-optimal,[6] albeit improved by metal promoters such as Mo.[7] Ni atoms are broadly recognized as excellent water dissociation centers. In contrast, Mo atoms have superior hydrogen adsorption properties.[7c] MoNi-based alloy electrocatalysts effectively reduce the energy barrier and speed up the sluggish HER kinetics. They have also been regarded as a benchmark non-Pt catalyst for HER. However, the strong Mo-H binding energy hinders the desorption of adsorbed H* from forming H_2, severely deteriorating the electrochemical HER activity.[8] In addition, the HER overpotential of MoNi catalysts tends to increase dramatically at high current densities (e.g., 500–1000 mA cm^{-2}) that are required for industrial electrolyzers.[7c] Therefore, new strategies are highly desired to enhance the activity of MoNi catalysts.

Stacking fault (SF) defect on the metal structures is a typical crystallographic defect, which is effective in directly tuning the surface atomic and electronic structure to alter the intrinsic reactivity of nanocrystalline materials.[9] Specifically, SF defect interrupts the proper order of stacking planes and creates lattice distortion regions (with abundant twins, steps and corner atomic structures) by stabilizing dislocations, which could induce strain and modulate the electronic structure of the materials.[10] The induced strain can tailor the binding energy of metal center-reactant intermediates, thus accelerating the production and desorption of the products (e.g., hydrogen).[11] Jiang et al.[9a] synthesized Ru nanoparticles with abundant SF through ultrafast heating with rapid quenching method to improve the water splitting performance with a low cell voltage of 1.51 V to deliver 10 mA cm^{-2} in 0.5 M H_2SO_4. The d-band center of Ru was found to be adjustable by the tensile and compressive strain induced by SF to achieve the optimal binding strength of adsorbate molecules during the water splitting reaction, thus enhancing the electrocatalytic performance. Unlike most vacancy defects that are generated by thermal equilibrium with a small population (e.g., 10^{-8} to 10^{-4}), disordered and unstable features, SF defects can be generated on the metallic nanostructures in a considerably large quantity in an ordered manner.[12] Most importantly, the SF defects are more stable than irregular vacancy defects since they have less energy deviation of vacated nanostructures from densest-packed ground-state geometries.[13] The metals with relatively low SF energy (γ_{SFE}) (e.g., Ag with the lowest γ_{SFE} of 16 mJ m^{-2}) tend to form SF easily,[10] while the metals with higher γ_{SFE} (e.g., Ni of 125 mJ m^{-2} and Mo of 569 mJ m^{-2}) are difficult to generate SF with conventionally mild strategies.[14] It is essential to develop facile and mild synthetic methods to create SF in high γ_{SFE} metals and alloys like MoNi to tune the metallic electronic and atomic structures and optimize their electrochemical activities.

Here, we show a combined chemical and thermal reduction route to generate large numbers of SF defects on the ultrathin MoNi nanosheets uniformly grown on Ni foam (d-MoNi). The high density of SF provides an ultra-high fraction of active sites and optimized electronic structure that significantly enhances the inherent HER activity of d-MoNi catalyst. The d-MoNi demonstrates excellent long-term durability under continuous testing for 100 h at high current densities of 1000 mA cm^{-2} in 1 M KOH electrolyte. Considering the high activity, durability, and low cost, d-MoNi modified with SF defects shows excellent potential as an alternative to commercial Pt catalysts for green hydrogen production.

2. Results and Discussion

2.1. Synthesis and Characterization

We designed the Mo-Ni electrodes by hydrothermal treatment of nickel foam into nickel nitrate ($Ni(NO_3)_2{\cdot}6H_2O$) and ammonium molybdate tetrahydrate aqueous solution ($(NH_4)_6Mo_7O_{24}{\cdot}4H_2O$) at 150 °C for 15 h to grow $MoNiO_x$ mixed metal oxide nanosheets on nickel foam. The SF defect-rich d-MoNi nanosheets were synthesized through a two-step reduction process. The first step involved etching in a sodium borohydride ($NaBH_4$) solution as the reducing agent. In the second step, a mixture of hydrogen and argon gas was used for reduction at 400°, 500°, and 600 °C with a constant ramp rate of 5 °C/min. The resulting products were denoted as d-MoNi-400, d-MoNi-500, and d-MoNi-600, respectively. **Figure 1a** shows a simplified schematic of the synthesis process of the MoNi electrodes, as well as the atomic configuration with and without SF structure. Among them, d-MoNi-500, with the optimal electrocatalytic performance, was selected for further investigation, and it is referred to as d-MoNi for short. A defect-free MoNi was synthesized via a similar preparation procedure (calcination at 500 °C) without $NaBH_4$ treatment. The nanosheet morphology of MoNi (Figure 1b,c) and d-MoNi (Figure 1d,e) inherited the morphology of the hydrothermal products $MoNiO_x$ before reduction treatments (Figure S1, Supporting Information) as shown by scanning electron microscopy (SEM) results. The d-MoNi (Figure 1e) shows a rougher surface than MoNi (Figure 1c).

The high-resolution transmission electron microscopy (HR-TEM) images (**Figure 2a–c**; Figure S2, Supporting Information) and high-angle annular dark-field-scanning transmission electron microscope (HAADF-STEM) image (Figure 2d) of d-MoNi reveal the presence of a high density of SF defects (estimated to be 7.5 ± 2.5% via Image-J software, Table S1, Supporting Information) that interact with each other and confirm the postulated MoNi intergranular or transgranular fracture defect (Figure 1a). SFs are planer faults that may be created by either removing one or several atomic layers, or inserting one or several extra layers into the metal crystal (Figure 2b,c) particularly with face centered cubic (fcc) and hexagonal close-packed (hcp) structures under extreme environments (e.g., temperature, pressure, irradiation, strong acid/base etching solution).[10a,15] The formation of SF

C. Pozo-Gonzalo
Institute for Frontier Materials
Deakin University
Melbourne, VIC 3125, Australia
K. Dastafkan, C. Zhao
School of Chemistry
The University of New South Wales
Sydney, NSW 2052, Australia
E-mail: chuan.zhao@unsw.edu.au

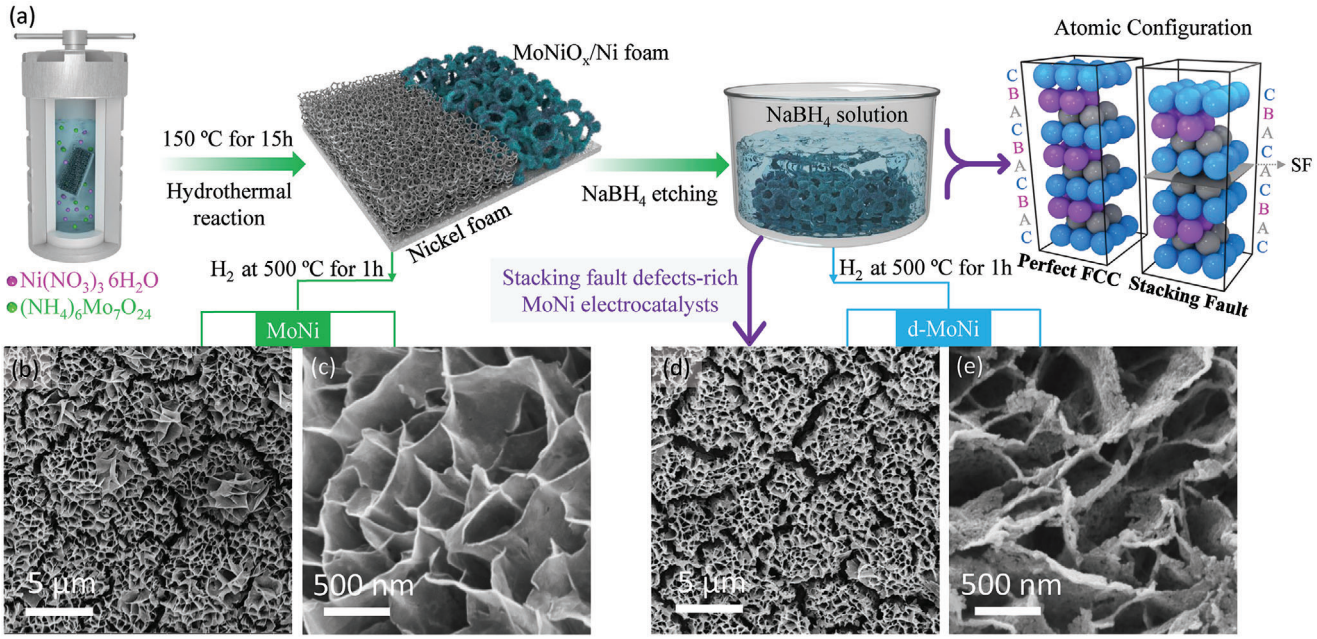

Figure 1. The preparation procedure and morphology. a) illustration of preparation procedure for MoNi and d-MoNi electrocatalysts and atomic configuration of $MoNi_4$ without and with SF, SEM images of b,c) MoNi and d,e) d-MoNi.

in d-MoNi involves (i) $MoNiO_4$ precursor solid dissolution in the $NaBH_4$ reducing agent solution (partial Ni leaching process: $MoNiO_4+NaBH_4+(3-\delta)H_2O \rightarrow NaBO_2+MoO_3+Ni(OH)_2+(4-\delta)H_2$), and (ii) disruption of the ordering of the surface atomic assembly by lattice dislocation during the thermal treatment under reduction condition. It suggests an arbitrary orientation interface in which adjacent ions are partially but regularly matched (Figure 2d; Figure S2f, Supporting Information). The TEM studies of d-MoNi samples annealed at varying temperatures (Figure S3, Supporting Information) indicate a strong correlation between the annealing temperatures and the density of SF. Specifically, at low temperature of 400 °C, d-MoNi-400 has a SF density of 10.5 ± 3.0%, whereas the SF density of d-MoNi-600 (annealed at 600 °C) decreases to 2.0 ± 1.5% (Table S1, Supporting Information). In contrast, MoNi without $NaBH_4$ treatment shows ordered lattice orientation and no obvious SF defects are observed (Figure S4, Supporting Information). During the nucleation/growth of d-MoNi, the $NaBH_4$ solution appears responsible for creating high concentration of Ni metal vacancies in the $MoNi_4$ alloy. This process facilitates the formation of ordered Ni vacancies and, thus the creation of SFs. The vacancy order is confirmed by observing crystal growth artifact formation of kinks, steps, and corners at the terminations of the SFs (Figure S5, Supporting Information), which are proper adsorption and reaction sites for molecule chemistry.[16]

Powder X-ray diffraction (XRD) pattern evidence reflections characteristic of tetragonal $MoNi_4$ phase (JCPDS PDF 04-007-0562), which dominates the crystal structures of MoNi and d-MoNi (Figure 2e). MoO_2 (JCPDS PDF 04-008-2624) is another crystalline phase present in both samples. According to the phase quantification results (by X'pert Highscore software), d-MoNi has a more pronounced $MoNi_4$ metallic phase (≈58.0%) than MoNi (≈38.5%) in Table S1 (Supporting Information). A very small amount of $MoNiO_4$ residue is present in MoNi after the hydrogen reduction treatment of the $MoNiO_x$ complex (hydrothermal product composed of $MoNiO_4$ and MoO_3 as shown in Figure S6, Supporting Information). For d-MoNi samples calcinated at different temperatures, the metallic phase of $MoNi_4$ increases with the temperature (Figure S7 and Table S1, Supporting Information). It is worth noting that the peak position of $MoNi_4$ in d-MoNi (see enlarged (211) peak in Figure 2f) shifts to a higher degree compared to the MoNi sample, while MoO_2 (see enlarged (220) peak in Figure 2g) has no peak shift, indicating the lattice distortion of $MoNi_4$ in d-MoNi. This can be confirmed by closer analysis of SF defects in the HR-TEM results (Figure 2a–d). Furthermore, the XRD peak shifts are considered definitive using Rietveld refinement of the XRD pattern. The strain rate calculation is summarized in Table S2 (Supporting Information), which indicates the presence of a 4.1% compressive strain in SF-enriched d-MoNi and only 0.2% compressive strain in MoNi. Notably, the strain rate in SF-enriched d-MoNi samples decreases with increasing calcination temperature. This observation aligns with previous reports and highlights the correlation between defect density (and induced strain) and annealing temperatures.[9b,10a] The correlation between strain and electrocatalytic activity was established theoretically by Hammer and Nørskov.[17] Residual strain can alter surface energy and lattice energy of nanomaterials, which correlate with key electrocatalytic processes, such as the adsorption/desorption of reaction intermediates and the charge transfer.[11b] The MoNi (8.7 nm for $MoNi_4$ and 7.9 nm for MoO_2) and d-MoNi (8.6 nm for $MoNi_4$ and 8.8 nm for MoO_2) have similar grain sizes calculated by the Scherrer equation (Table S2, Supporting Information), precluding the contribution of size effect on the electrocatalytic performance.

The surface composition of the MoNi and d-MoNi samples shown in X-ray photoelectron spectroscopy (XPS) profiles

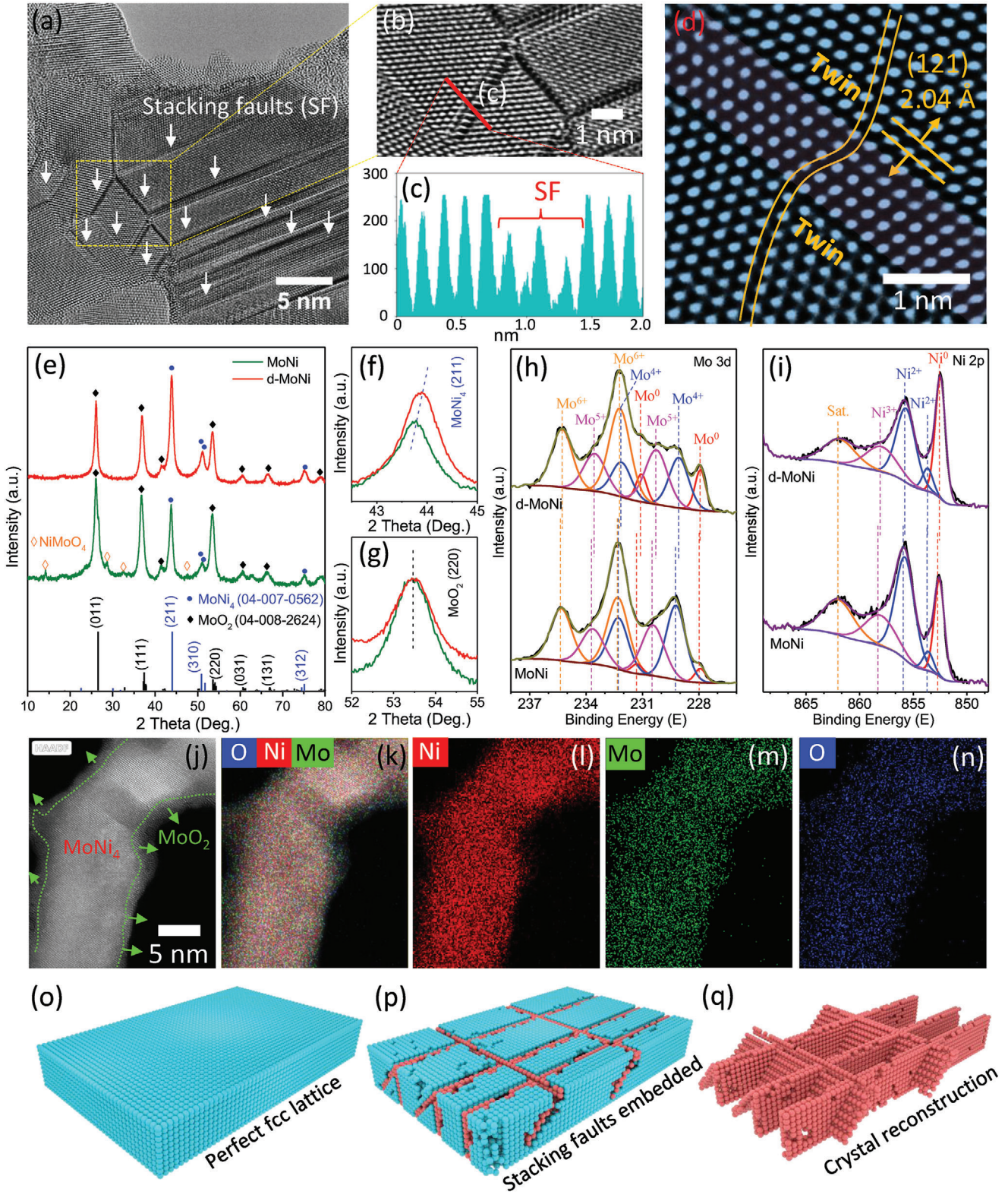

Figure 2. Structural and compositional characterizations. a,b) HR-TEM images of d-MoNi, c) line profiles of the red line in (b), d) colored HAADF-STEM image of d-MoNi, e) XRD patterns of MoNi, d-MoNi and standard XRD patterns of $MoNi_4$ and MoO_2, f,g) enlarged XRD patterns of $MoNi_4$ (121) and MoO_2 (220), XPS profiles of h) Mo 3d and i) Ni 3d of MoNi and d-MoNi, j) HAADF-STEM-EDS mappings of d-MoNi, where red represents Ni, green refer to Mo, and blue refers to O, schematic illustration of o) perfect fcc lattice, p) SFs embedded fcc lattice, and q) crystal reconstruction of SFs.

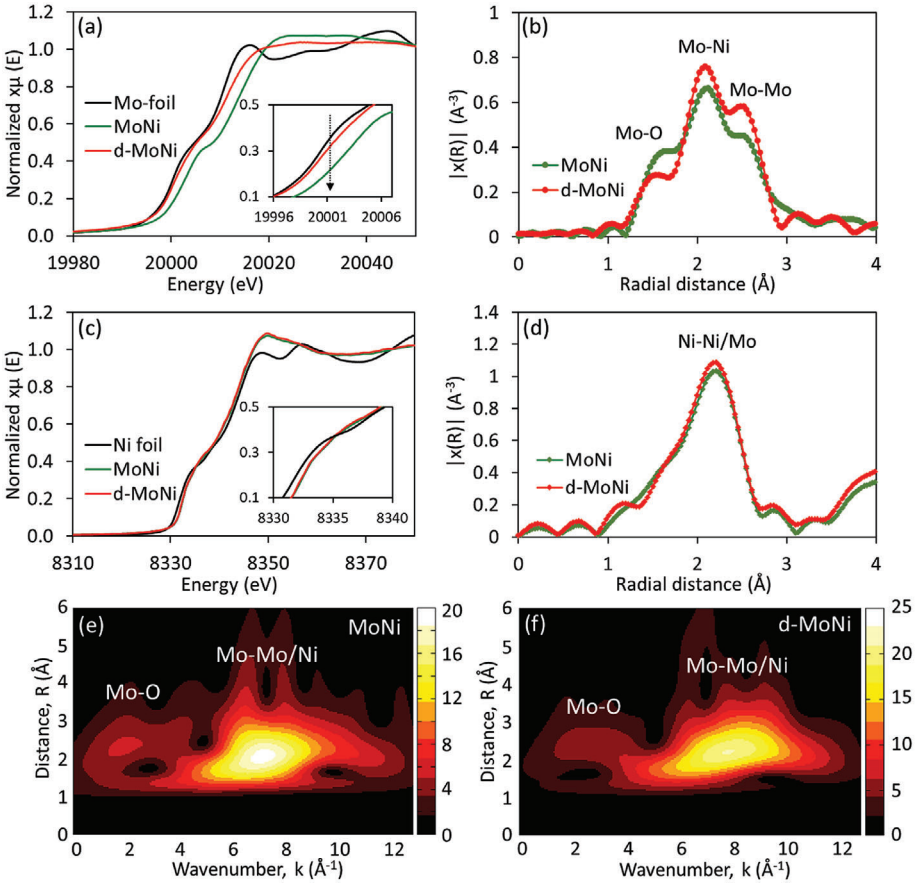

Figure 3. Structural and compositional characterizations. Displaying spectra of samples of MoNi and d-MoNi (with respective reference foil data) as a) Mo K-edge XANES spectra, b) Fourier Transform Mo K-edge EXAFS spectra, c) Ni K-edge XANES spectra, d) Fourier Transform Ni K-edge EXAFS spectra, and Mo K-edge EXAFS 2D plots of wavelet transform of e) MoNi and f) d-MoNi.

(Figure 2h,i) indicates the coexistence of metallic (Mo^0 and Ni^0) and oxidized phases (Mo^{4+}, Mo^{5+}, Mo^{6+}, Ni^{2+} and Ni^{3+}), which contrasts with the oxidized phase composition of the $MoNiO_x$ precursors before reduction treatment (Ni^{2+}, Ni^{3+} and Mo^{6+} in Figure S8, Supporting Information). It is noted that d-MoNi ($Mo^0/(Mo^{(4,5,6)+}) = 0.11$, $Ni^0/(Ni^{(2,3)+}) = 0.51$) obtained by two-step reduction (chemical and hydrogen reduction) has more pronounced metallic phase than MoNi ($Mo^0/(Mo^{(4,5,6)+}) = 0.04$, $Ni^0/(Ni^{(2,3)+}) = 0.34$) by one-step reduction (hydrogen reduction), the result of larger amount of metallic phases (Mo^0 and Ni^0) in d-MoNi has corresponded with XRD results (Figure 2e).

It is worth noting that the d-MoNi has more surface Mo than MoNi by comparing the peak ratio of Mo/Ni (by XPS survey in Figure S9, Supporting Information), where d-MoNi (5.4) > MoNi (5.2). It is speculated that the formation of SFs in d-MoNi is through the dislocation/missing atomic line of Ni, resulting in twin, step, and dislocation defects in the d-MoNi (Figure 2a–d; Figure S2, Supporting Information). The Mo and Ni spectra of d-MoNi were blue-shifted to lower binding energies than MoNi (Figure 2h,i). Specifically, the oxidized Mo species (4+, 5+, and 6+) show respective shifts of 0.18, 0.17, and 0.07 eV to lower binding energy, while the metal species of Mo^0 has a blue shift of ≈0.14 eV. Further, the Ni 2p of d-MoNi exhibits a blue shift of ≈0.10 eV for all three Ni^0, Ni^{2+}, and Ni^{3+} species. These results suggest that the electrons from Mo and Ni accumulate near SFs in d-MoNi. This accumulation is beneficial in weakening the binding strength of Mo(Ni)-H, thereby facilitating the desorption of H_2 and ultimately increasing the HER efficiency.[18] This has been corroborated by H_2 temperature programmed desorption (H_2-TPD) results (Figure S10, Supporting Information), where the desorption peak temperatures of d-MoNi are lower than MoNi for both weakly chemisorbed H_2 (145 °C < 165 °C) and strongly chemisorbed H_2 (629 °C < 654 °C) on the surfaces, indicating an enhanced H_2 desorption capacity. The HAADF-STEM-energy-dispersive X-ray spectrometry (EDS) mapping results (Figure 2j–n; Figure S11, Supporting Information) further demonstrate the coexistence of MoNi metal alloys and Mo oxides phases, where Mo oxides surround MoNi alloys. The schematic illustration of the perfect fcc crystal structure of MoNi alloy, SFs embedded fcc crystal structure of MoNi, and crystal reconstruction of SFs are shown in Figure 2o–q.

X-ray absorption spectroscopy (XAS) was collected at Mo K-edges and Ni K-edges for MoNi and d-MoNi samples. **Figure 3a** presents the X-ray absorption near-edge structure (XANES) spectra of MoNi and d-MoNi at Mo K-edge. The d-MoNi is much more akin to the Mo foil in terms of edge position, while the MoNi is shifted to higher energy. This suggests that the d-MoNi is more metallic in nature, like the foil over the MoNi. The radial

structure function around Mo was determined by Fourier transform (FT) of extended X-ray adsorption fine-structure (EXAFS) spectra and fittings (Figure 3b; Figures S12–14, Supporting Information). The Mo-edge EXAFS fittings containing the path, coordination number (CN), and bond distance are summarized in Table S3 (Supporting Information). The peaks at 2.03 (1.99), 2.54 (2.53), and 2.74 (2.70) Å are associated with Mo-O, Mo-Ni, and Mo-Mo bonds in MoNi (and d-MoNi).[19] Comparing the Mo K edge EXAFS (Figure 3b), there are distinctive changes in the amplitudes of the peaks in the FT. The fitting of the MoNi samples suggests that MoNi has a higher degree of molybdenum oxide (CN (Mo-O) = 0.79) over that of the d-MoNi (CN (Mo-O) = 0.43), and consequently, there is a higher degree of metallic bonding in the defective d-MoNi (CN (Mo-Mo) = 2.48, CN (Mo-Ni) = 2.09) than MoNi (CN (Mo-Mo) = 1.79, CN (Mo-Ni) = 1.99). Especially, the first-shell Mo-Mo CN of d-MoNi (2.48) is much higher than MoNi (1.79). This indicates that where a more oxygenated species is formed, reduction with $NaBH_4$ removes more oxides in the material forming a more integrated metallic alloy species. The observance of defects could result from the structural changes required to form more Mo-Mo bonding, resulting from the loss of the oxides and possible dissolution of Ni. In addition, the Mo-Mo bonding in d-MoNi is slightly compressed compared to MoNi, suggesting the presence of compressive strain in d-MoNi that is attributed to the formation of high density of SF defects. Analysis of the Ni K-edge XAS of MoNi and d-MoNi shows no significant differences in the XANES or the EXAFS (Figure 3c,d). The fitting analysis (Figures S15–S17 and Table S4, Supporting Information) suggests that both MoNi and d-MoNi spectra are dominated by Ni-Ni (CN = 4.1 and 4.0) bonding fitting with no Ni-O bonding being prevalent.[20] No Ni-Mo backscattering signal was found due to the dominance of Ni-Ni backscattering.

The results from the Mo-K edge EXAFS 2D plots of wavelet transform (2D-WT) (Figure 3e,f; Figure S18, Supporting Information), an emerging method to discriminate backscattering atom types in FT EXAFS data, indicate the presence of a light atom scatterer in the non-defective MoNi sample at ≈2.5Å in r-space and ≈2 $Å^{-1}$ in k-space. When compared with the 2D-WT of Mo-O (Figure S19a, Supporting Information), the absence of features at low k and higher r in the wavelet transform of the non-defective MoNi indicates that there are only surface Mo-O in the MoNi. The Mo foil reference data (Figure S19b, Supporting Information) indicates that Mo-Mo scattering should scatter at a higher k of ≈8 $Å^{-1}$. The d-MoNi has a slightly more spread-out contribution to higher k, reflecting a greater degree of Mo-Mo scattering when compared to the MoNi sample (Figure 3e,f), and agrees with the EXAFS fit analysis (Figures S13 and S14, Supporting Information). As expected from Ni K-edge EXAFS, the MoNi and d-MoNi have similar 2D-WT almost identical to Ni foil (Figure S20, Supporting Information).

2.2. Formation Mechanism of SF

To characterize the experimental structural changes, the crystal structures of pristine $MoNi_4$, experimental $MoNi_4$, and d-$MoNi_4$ samples were simulated using CrystalMaker Software. The resultant simulated crystal structure, electron diffraction (ED), and XRD data for $MoNi_4$, and d-$MoNi_4$ relative to pristine $MoNi_4$ were generated by varying the following: (i) particulate strain, (ii) unit cell volume contraction/expansion, (iii) preferred orientation, and (iv) Ni metal vacancy concentration, as shown in **Figure 4a–d**. Further, the data derived from the simulation were studied comparatively, as tabulated in Table S5 (Supporting Information). The simulated XRD pattern for pristine $MoNi_4$ (Figure 4e) shows that the $(2\bar{1}1)$ and (310) peaks are positioned at 2θ angles of 43.59° and 50.76°, and the peak intensity ratio is $\frac{I_{(2\bar{1}1)}}{I_{(310)}} = 2.27$, all of which are identical to those reported for the reference XRD pattern (The International Centre for Diffraction Data (ICDD) 04-007-0562). In contrast, the experimental XRD pattern for pristine $MoNi_4$ (Figure 4e) shows that the $(2\bar{1}1)$ and (310) peaks shift to the higher 2θ angles of 43.67° and 50.85°, and there is a significant increase in $\frac{I_{(2\bar{1}1)}}{I_{(310)}}$ to 4.14, thus indicating lattice contraction owing to Ni removal and resultant vacancy formation. This contraction derives from a combination of the lattice shrinkage due to the removal of Ni from the $(2\bar{1}1)$ plane and the lattice expansion due to the charge-compensating $2Mo^{5+} \rightarrow 2Mo^{4+}$ reduction on the (310) plane (Figure 2h,i). The ionic radius of Ni^{2+} in its twofold coordination in $MoNi_4$ is estimated to be 0.056 nm based on analogy with the Hg^{2+} ion.[21] The ionic radius of Mo^{5+} in its eightfold coordination is estimated to be 0.085 nm by analogy with $Cr^{5+,}$ and the equiv. ionic radius of Mo^{4+} is estimated to be 0.094 nm by analogy with V^{4+}. Since 0.056 nm is more than six times the difference between the radii of the two Mo valences (0.009 nm), the significant lattice contraction can be attributed to the formation of Ni vacancies. I.e., a comparison between simulated pristine $MoNi_4$ and the experimental XRD patterns revealed no difference in particulate strains but, for the latter, –0.517% lattice strain (contraction), predominant $(2\bar{1}1)$ crystallographic orientation (36.66%), and 5% Ni vacancies.

The simulated XRD pattern for d-$MoNi_4$ (Figure 4e) shows that the $(2\bar{1}1)$ and (310) peaks are positioned at respective 2θ angles of 43.96° and 51.20°, and a peak intensity ratio is reduced to $\frac{I_{(2\bar{1}1)}}{I_{(310)}} = 3.70$. Compared to pristine $MoNi_4$, these parameters are generated in d-$MoNi_4$ by 0.1% particulate strain, –2.40% lattice strain (contraction), predominant $(2\bar{1}1)$ crystallographic orientation (32.00%) and 22.00% Ni vacancies. It has been reported that Ni vacancies cause a significant reduction in generalized SF.[22] At high vacancy concentrations, both stable and unstable SF energies drop significantly, thereby forming these defects.[23] The presence of SFs can lead to anisotropic growth of the $MoNi_4$ structure, which is concluded to be the driving force for the progressive intensity variations between $(2\bar{1}1)$ and (310), as confirmed in other materials.[24] The shifts in all four structural variables relative to those for pristine $MoNi_4$ are consistent with the generation of increasing SF concentrations in d-$MoNi_4$. These data suggest that the decrease in the predominance of the $(2\bar{1}1)$ crystallographic orientation from 36.66% to 32.00% in favor of increasing (310) orientation represents a comparative but quantifiable estimate of the SF density.

2.3. Electrocatalytic Performance

The electrocatalytic performance of HER was tested using a standard three-electrode system in 1 M KOH. The linear sweep voltammetry (LSV) curves shown in **Figure 5a** (corresponding

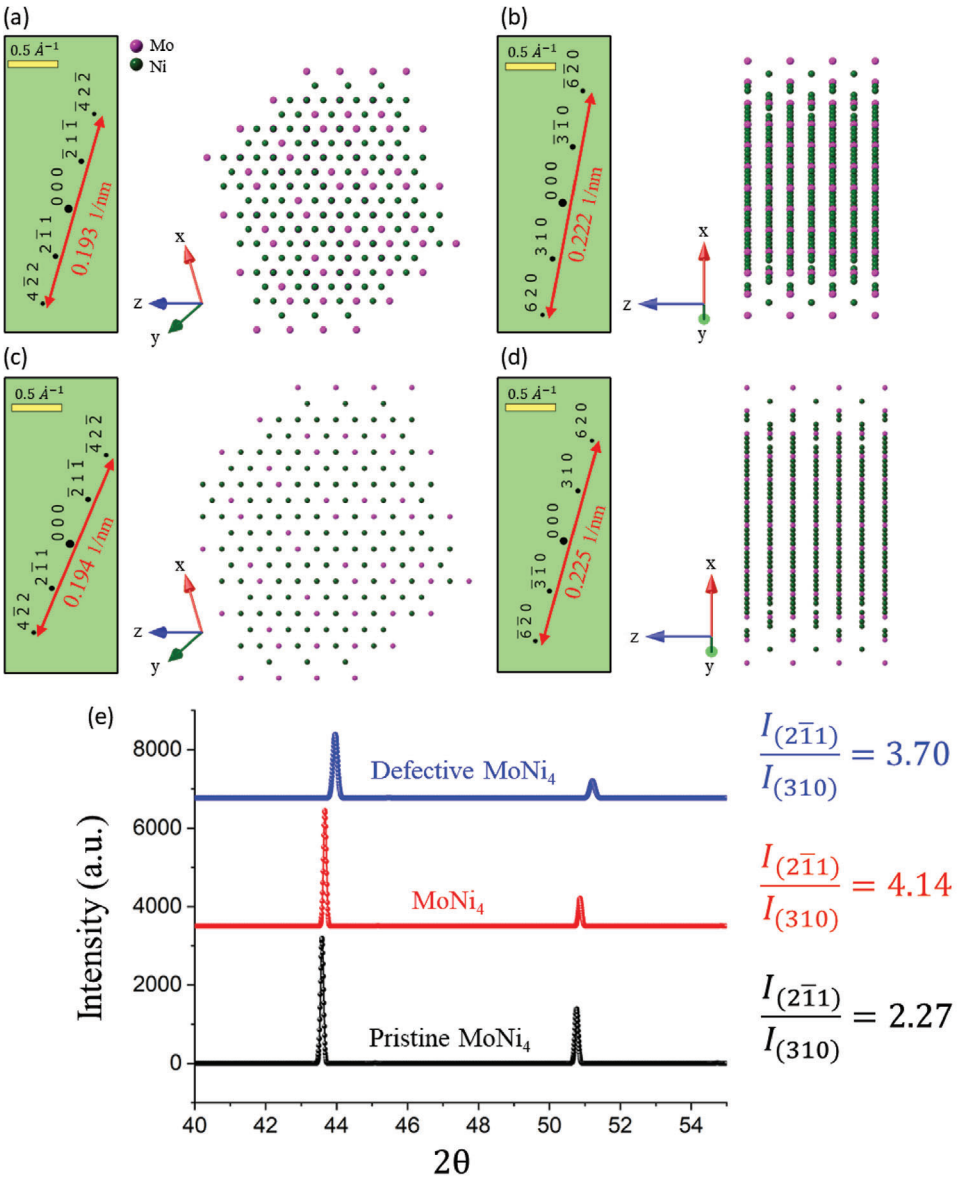

Figure 4. Crystal structure simulations. Simulated crystal structure, selected area electron diffraction (SAED), and XRD data for $MoNi_4$, and d-$MoNi_4$ relative to pristine $MoNi_4$; a,b) SAED patterns and simulated lattice fringes perpendicular to (211) and (310) planes of pristine $MoNi_4$, respectively; c,d) SAED patterns and simulated lattice fringes perpendicular to (211) and (310) planes of d-$MoNi_4$, respectively; e) simulated XRD patterns for pristine $MoNi_4$, experimental pristine $MoNi_4$, and experimental d-$MoNi_4$.

LSV curves without *iR* compensation shown in Figure S21, Supporting Information) indicate that the HER activity of MoNi after thermal hydrogen reduction is significantly improved compared with MoNi oxides ($MoNiO_x$ and d-$MoNiO_x$), requiring the overpotentials of 235 and 349 mV to reach current densities of 500 and 1000 mA cm^{-2}, respectively (Table S6, Supporting Information). This confirms that MoNi alloy is more active than MoNi oxides, which is consistent with previous theoretical results that $MoNi_4$ has much better HER performance than MoO_2.[7c] The d-MoNi with additional $NaBH_4$ reduction before H_2 reduction shows further considerable improvement in HER activity (Figure 5a). Table S6 (Supporting Information) highlights the notable enhancement in overpotential (η) for d-MoNi, requiring only 78 and 121 mV to reach current densities of 500 and 1000 mA cm^{-2}, respectively, which also significantly outperforms the benchmark 20% Pt/C (300 mV at 500 mA cm^{-2}). In Table S6 (Supporting Information), the turnover frequency (TOF) of d-MoNi at η of 50 and 100 mV is 2.7 and 8.7 s^{-1}, which are approximately four times higher than MoNi (0.7 and 1.7 s^{-1} at η of 50 and 100 mV, respectively), and both d-MoNi and MoNi are superior to 20% Pt/C (0.7 and 1.3 s^{-1} at η of 50 and 100 mV, respectively). Regarding the d-MoNi samples annealed at different temperatures (Figure S22, Supporting Information), d-MoNi-500 surpasses d-MoNi-600 due to its higher density of SF defects (7.5 ± 2.5% > 2.0 ± 1.5%), despite the former having a lower $MoNi_4$ phase composition (75.3% for d-MoNi-400 compared to

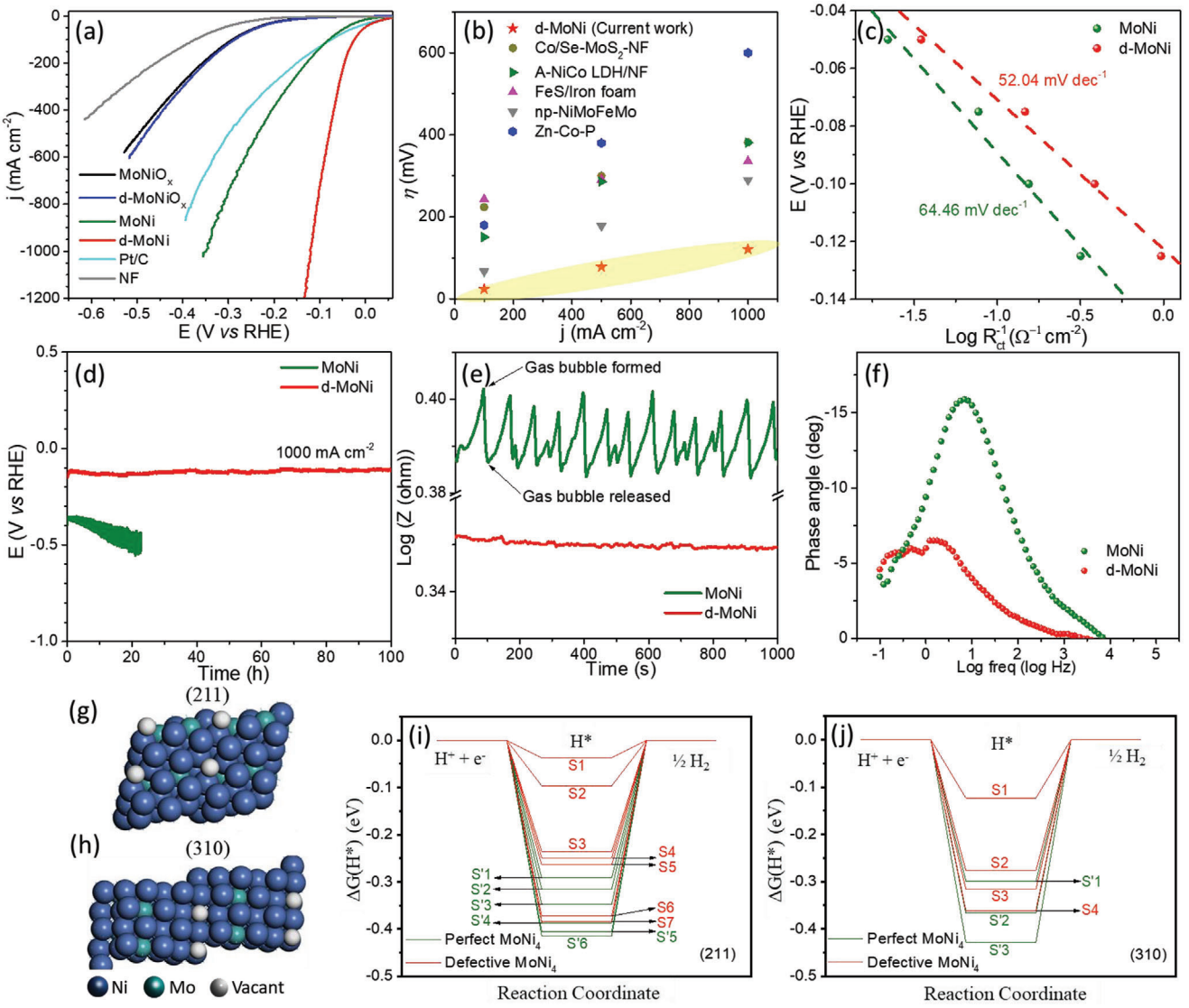

Figure 5. Catalytic performance of HER: a) LSV curves of MoNi, d-MoNi, $MoNiO_x$, and d-$MoNiO_x$, 85% ohmic potential (*iR*) compensation, b) current density j versus overpotential η of d-MoNi compared to literature ((i),[27a] (ii),[31] (iii),[32] (iv),[33] and (v)[34]), c) semi-logarithmic plot of the inverse charge-transfer resistance, R_{ct}^{-1}, as a function of potential, d) chronopotentialmetry of MoNi and d-MoNi at 1000 mA cm^{-2} in 1 M KOH, 85% *iR* compensation, e) dynamic specific resistance variation at a potential of −0.1 V versus RHE and frequency of 10000 Hz, f) Bond-phase angle plots at a potential of −0.1 V versus RHE and frequency range of 0.1–100000 Hz, atomic structural models of g) $MoNi_4$ (211) surface and h) $MoNi_4$ (310) surface, calculated adsorption free energy diagram for the Tafel step of perfect and defective $MoNi_4$ on i) (211) surface and j) (310) surface.

58.0% for d-MoNi-500). In contrast, the moderate HER activity of d-MoNi-400 can be attributed to the low annealing temperature of 400 °C and associated reduced effectiveness of the H_2 reduction. This results in the lowest $MoNi_4$ content (29.3%) despite its high SF density (10.5 ± 3.0%). In effect, the greater metal oxide content in d-MoNi-400 forms a greater extent of insulating oxide layer on the $MoNi_4$ surface, which can hinder the access of H_2O to the active sites and thus reduce the HER performance. At temperatures that are too high (i.e., 600 °C), too many SFs are eliminated, whereas at temperatures that are too low (i.e., 400 °C), the reaction to form $MoNi_4$ is incomplete. Thus, a temperature of 500 °C achieves a balance between the completion of the reduction reaction and the elimination of SFs, resulting in a sufficient amount of $MoNi_4$ with sufficient SFs density to yield maximal performance.

To ensure a fair comparison, we normalized the HER activity based on the mass loading of $MoNi_4$. As depicted in Figure S23a (Supporting Information), all d-MoNi samples with varying content of SF defects exhibit better mass activity than the MoNi sample without SF, indicating an improvement in the intrinsic activity of $MoNi_4$ upon the introduction of SF. Figure S23b (Supporting Information) illustrates a direct dependence between SF density and HER performance, where the d-MoNi-400 with the highest SF density displays the best mass activity (Table S7, Supporting Information). The Faraday efficiency of hydrogen production on d-MoNi is 100.9 ± 1.7% (Table S8, Supporting

Information), suggesting that the generated current is completed due to the HER. As shown in Figure S24 (Supporting Information), the Tafel slopes of d-MoNi and MoNi are 27 and 33 mV dec^{-1}, respectively, which are smaller than that of Pt/C (38 mV dec^{-1}). The Tafel slope, reflecting the logarithmic relationship between the reaction rate and overpotential, serves as an indicator of catalytic performance. The smaller Tafel slope exhibited by d-MoNi implies an improved HER reaction rate compared to MoNi and Pt/C. Tafel slopes close to 30 mV dec^{-1} are often associated with Tafel step as rate-determining steps (rds), suggesting the rds for MoNi and d-MoNi catalysts may correspond to Tafel step.[25] The exchange current densities (j_0) are calculated as 0.086 mA cm^{-2} and 0.066 mA cm^{-2} for d-MoNi and MoNi, respectively. The reaction barrier, indicated by the j_0, is significantly lower for d-MoNi (0.086 mA cm^{-2}) compared to MoNi (0.066 mA cm^{-2}), suggesting that d-MoNi facilitates the HER more efficiently and with less resistance. This difference implies that d-MoNi offers a more favorable kinetic profile for initiating the HER than d-MoNi. In comparison to recently published state-of-the-art HER catalysts, d-MoNi exhibits superior activity, evidenced by significantly smaller overpotentials at 100 mA cm^{-2} and a lower Tafel slope (Figure S25a and Table S9, Supporting Information), as well as high current density of 1000 mA cm^{-2} (Figure 5b). In order to eliminate the influence of Ni foam substrate on the HER activity, the catalysts were drop-casted on a glassy carbon microdisc electrode, and the activity was evaluated. The trends observed in Figure S26 (Supporting Information) are consistent with those of NF-based electrodes. Specifically, the d-MoNi demonstrates the highest activity, followed by Pt/C and the MoNi. Further, d-MoNi displays a very low overpotential of 32 mV at 10 mA cm^{-2}, significantly outperforming previous studies (Figure S25b and Table S9, Supporting Information), which attests to its high intrinsic activity. When compared specifically to MoNi-based electrocatalysts reported in the literature, the superior performance of the d-MoN becomes evident (as illustrated in Figure S27 and Table S10, Supporting Information). This result underscores the specific impact of SFs in achieving such exceptional HER activity, setting this work apart from previous studies. Electrochemically active surface area (ECSA) was also estimated for both d-MoNi and MoNi through double-layer capacitance (C_{dl}) (Figure S28, Supporting Information) and used to normalize the recorded apparent current density (Figure S29a, Supporting Information). Notably, d-MoNi exhibits a low overpotential of 100 mV at a current density of 0.5 mA cm^{-2}, further confirming its high intrinsic activity, ranking it one of the best catalysts reported for HER so far (Figure S29b and Table S11, Supporting Information).

The Nyquist plots (Figure S30, Supporting Information) show that the d-MoNi has a significantly lower charge transfer resistance (R_{ct}) (indicated by the smaller semicircle diameter in the Nyquist plots) than that of MoNi, indicating that d-MoNi exhibits better electronic conductivity and hence lower resistance to fast-electron transfer. Early investigation into the dependence of the obtained impedance with applied potentials has demonstrated that the gradient of $\log(R_{ct}^{-1})$ versus potential corresponds to the Tafel slope of the proton discharging step.[26] The potential is plotted versus the $\log(R_{ct}^{-1})$, yielding a linear dependence, as shown in Figure 5c. The slope of d-MoNi (52 mV dec^{-1}) is much smaller than the MoNi (64 mV dec^{-1}), indicating a much faster proton discharge kinetics.

Stability is another very important property required of HER catalysts for practical applications, but most non-precious metal-based catalysts tend to dissolve or mechanically exfoliate into alkaline electrolytes, resulting in unsatisfactory stability. The defective d-MoNi shows outstanding long-term stability, remaining stable for 100 h at a current density of 1000 mA cm^{-2}, while MoNi rapidly loses activity within 20 h (Figure 5d). This good stability at high current density (1 A cm^{-2}) in alkaline electrolytes has rarely been reported in the literature (Table S12, Supporting Information).[19,27] The multistep chronopotentiometry curves of d-MoNi at current densities ranging from 50 to 400 mA cm^{-2} in Figure S31 (Supporting Information) show that the electrocatalytic activity remains stable at each step and can recover the original potential after 4 cycles (200 h in total). To elucidate the reason for the excellent stability of d-MoNi catalyst, we have conducted the operando gas bubble evolution by monitoring the dynamic variation of the resistance component of impedance during HER (at a potential of −0.1 V vs RHE).[28] The plots shown in Figure 5e depict a smooth curve of d-MoNi and a fluctuating periodical curve of MoNi (where the tops of the peak represent the formation and accumulation of bubbles and the bottoms of the peaks depict the release of bubbles). This suggests the sluggish growth and release of gas bubbles (H_2) on the surface of MoNi, while rapid gas evolution occurs on the surface of d-MoNi. The Bond-phase angle plot of MoNi in Figure 5f exhibits classical single-time-constant behavior (electrical equiv. circuit models in Figure S30, Supporting Information). d-MoNi shows a two-time-constant model consisting of a series resistance, R_s, in series with two parallel branches, related to the charge-transfer process (C_{d1}-R_t) and surface defect (C_{d2}-R_d), respectively (electrical equiv. circuit models in Figure S30, Supporting Information), which usually reveals the response of the HER on rough electrode surfaces.[26] It explains the observed fast bubble evolution phenomenon (Figure 5e) on the rough surfaces of d-MoNi caused by the high density of SF defects, which is responsible for the fast HER and excellent stability. The post-reaction microscopic characterizations of SEM and HR-TEM were carried out, where d-MoNi have the nanoflake morphology remain well (Figure S32, Supporting Information), and the SF defects remain (7.0 ± 1.8%) after the stability testing (Figure S33, Supporting Information). The XPS results for the d-MoNi after stability testing (Figure S34, Supporting Information) show surface oxidation states similar to those of the fresh d-MoNi (Table S13, Supporting Information), with only Ni^0 (the ratio of $Ni^0/Ni^{2+/3+}$ from 0.51 to 0.17) decreasing after the stability test, which is attributed to the surface oxidation when exposure to air during drying process at 80 °C before conducting the XPS measurements.

It is necessary to understand the role of defective sites in d-MoNi for the significant enhancement of HER activity, therefore, we further performed the DFT calculations. According to the kinetic result by Tafel plots (Figure S24, Supporting Information), the rate-determining step for MoNi catalysts is Tafel step ($H^* + H^+ + e^- = H_2 + *$).[7c] According to the Sabatier principle, a catalyst with high HER performance should bind an H atom neither too weakly nor too strongly, an ideal hydrogen adsorption-free energy is zero. Thus, we calculated the Gibbs free energy (ΔG_H) on multi-adsorption sites on the three facets ((310), (211), and (312) according to XRD results) of perfect and defective $MoNi_4$ (Figure 5g–j; Figure S35, Supporting Information). The

specific adsorption sites are presented in the annotated structural diagrams in Figures S36–S41 (Supporting Information), and the ΔG_H values corresponding to specific active sites are listed in Table S14 (Supporting Information). It shows that the ΔG_H values are much lower on defective $MoNi_4$ (e.g., −0.03 eV on S1 of (211) and −0.12 eV on S1 of (310)), than on perfect $MoNi_4$ (e.g., −0.29 e V on S'1 of (211) and −0.30 eV on S'1 of (310)) (Figure 5g–j; Table S14, Supporting Information), which is even lower than the highly efficient Pt catalyst (−0.09 eV).[29] The (312) facet is a high-index facet with a steps atom-dominated surface (similar configuration to SF defects) that is intrinsically active for chemical adsorption and catalytic reactions[30] and has a very low ΔG_H value of −0.03 eV, nearly close to the optimal zero value (Figure S35 and Table S14, Supporting Information). These results confirm that the SF defects in d-MoNi have provided optimized absorbance sites, which decrease the H_2 adsorption energy and accelerate the H_2 dissociation from the catalyst surface, thus improving the electrocatalytic kinetics of HER.

3. Conclusion

In summary, a two-step reduction protocol was developed for fabricating SF defects-rich MoNi electrocatalysts (d-MoNi) exhibiting exceptionally high activity and stability for alkaline HER. The defect-rich d-MoNi exhibits enormously enhanced intrinsic activity, with nearly four times higher turnover frequency than non-defective MoNi and commercial Pt/C catalysts. The adjusted electronic structure derives the excellent HER performance of d-MoNi through compressive strain induced by the formation of SFs in the MoNi lattice, which toilers the hydrogen adsorption energy and facilitates the dissociation of hydrogen, thus enhancing the electrocatalytic hydrogen evolution. The d-MoNi catalyst also shows no obvious deactivation over 100 h long-term stability test at a high current density of 1000 mA cm^{-2}, demonstrating its potential for applications in industrial water electrolyzers. The developed SF defect engineering strategy is expected to inspire the preparation of many other defect-rich metal and metal alloys for achieving high-performance low-cost electrocatalysts for hydrogen evolution, as well as a number of important electrochemical reactions in energy conversion and storage devices.

4. Experimental Section

Materials: Nickel(II) nitrate hexahydrate ($Ni(NO_3)_2{\cdot}6H_2O$), ammonium molybdate tetrahydrate ($(NH_4)_6Mo_7O_{24}{\cdot}4H_2O$), Nafion 117 solution (≈5% in a mixture of lower aliphatic alcohols and water), and sodium borohydride ($NaBH_4$) were purchased from Sigma-Aldrich. Nickel foam (NF) with a thickness of 1.6 mm, bulk density of 0.45 g cm^{-3}, porosity of 95%, and purity of 99.5% was purchased from Goodfellow Cambridge Ltd.

Synthesis of d-MoNi Electrodes: 5.59 g $Ni(NO_3)_2{\cdot}6H_2O$ and 0.84 g $(NH_4)_6Mo_7O_{24}{\cdot}4H_2O$ were dissolved into 160 mL deionized water under stirred for 1 h to form a homogeneous solution. 40 mL of the solution was transferred into a 50 mL Teflon reactor, where a 1 cm × 2 cm NF (pre-washed with 3 M HCl and acetone) was placed into the solution. The Teflon reactor was sealed in a stainless-steel jacket and placed in an oven for hydrothermal reaction at 150 °C for 15 h. After the hydrothermal reaction, NF and precipitate inside the Teflon reactor were washed with ethanol and deionized water three times and dried at 80 °C for 24 h. Mo-Ni oxides nanoflakes were grown on the surface of the NF (denoted as $MoNiO_x$). The NF and dried precipitate powder were then dipped into $NaBH_4$ solution (4 mg $NaBH_4$ into 20 mL water) for 30 min before washing with water (centrifuge wash for powdered sample) and dried at room temperature for 24 h (denoted as d-$MoNiO_x$). It was then calcinated in a tube furnace in the conditions of 5 °C min^{-1}, at temperatures of 400°, 500°, and 600 °C, respectively for 1 h, 10 mL min^{-1} H_2, and 50 mL min^{-1} Ar, 1 bar, to obtain the d-MoNi on NF electrode and d-MoNi powdered sample. The samples calcinated at different temperatures were named as d-MoNi-400, d-MoNi-500, and d-MoNi-600, among which the optimal sample d-MoNi-500 was referred to as d-MoNi in the study. MoNi electrode was synthesized without the $NaBH_4$ treatment. The obtained $MoNiO_x$ was directly calcined in a tube furnace under 5 °C min^{-1}, 500 °C for 1 h, 10 mL min^{-1} H_2 and 50 mL min^{-1} Ar, 1 bar, to obtain the MoNi electrode.

Characterization: XRD analyses were performed on a PANalytical Empyrean II diffractometer with Cu Kα radiation (λ = 0.15406 nm) at 45 kV and 40 mA to identify the crystal phases and to analyze lattice parameters. Scattering intensity was recorded in the range of $10° < 2\theta < 80°$ for all of the samples with a 2θ step of 0.03° and a count time of 2 s per step. XRD testing was conducted on the MoNi and d-MoNi powdered samples due to the influence of the Ni substrate diffraction peaks on samples on nickel foam, where the diffraction peaks of $MoNi_4$ overlap with those of Ni. Diffraction patterns were indexed to JCPDS (Joint Committee on Powder Diffraction Standards) files. The morphology of the electrocatalysts was characterized by SEM and TEM by FEI Nova NanoSEM 450 FE and JEOL TEM-F200 systems, respectively. The HAADF-STEM and EDS were conducted employing a FEI Themis-Z image- and probe-corrected monochromated TEM, equipped with a SuperX EDS detector system for ultra-high-count rates operated at 300 kV. XPS was used to determine the Ni 2p and Mo 3d binding energies (BEs) of surface species. The analyses were performed using a Thermo Scientific, UK (model ESCALAB250Xi) using mono-chromated Al Kα ($h\nu$ = 1486.68 eV) as the excitation source with 120 W power (13.8 kV x 8 mA), 500 µm spot size. The C 1s peak at 284.8 eV for adventitious carbon was employed as the reference for energy alignment. The sample preparation for post-reaction characterizations (SEM, TEM, and XPS) was as follows: the d-MoNi electrode, which had undergone a stability test at 1000 mA cm^2 for 100 h in 1.0 M KOH, was rinsed with distilled water to eliminate the electrolyte. Then the electrode was dried at 80 °C for 12 h before conducting post-reaction characterization. To prepare the sample for the H_2-TPD test, 200 mg of sample was heated from room temperature to 500 °C at a rate of 20 °C/min in a gas mixture of 40 mL min^{-1} H_2/N_2 (10 vol% H_2) and held at 500 °C in the same atmosphere for 1 h to pretreat the sample. Next, the gas atmosphere was shifted to 40 mL min^{-1} N_2 at 500 °C for 1 h to clean the surface before decreasing the temperature to 50 °C. 40 mL min^{-1} H_2/N_2 (10 vol% H_2) was then introduced at 50 °C and kept for 1 h. The gas was shifted to 40 mL min^{-1} N_2, and the temperature program was increased from 50 °C to 900 °C at a rate of 20 °C/min, followed by a hold at 900 °C for 0.5 h. The TCD signal was recorded during the temperature profile to monitor H_2 desorption from the material. These experiments provide a direct measure of the hydrogen binding energy by analyzing the temperature at which hydrogen desorbs from the surface of the material.

X-Ray Absorption Spectroscopy Studies: The Mo K-edge X-ray absorption experiments were conducted at the Australian Synchrotron at the XAS Beamline, collected with single scans at 20 min each in fluorescence using a 36-element Ge fluorescence detector. Samples were diluted with boron nitride and mounted using Kapton tape inside a He purged cell held at room temperature. Sample spectra were collected up to k = 15 $Å^{-1}$ in parallel with their foil references. The Ni K edge X-ray absorption experiments were collected at Diamond Light Source, single scans at 20 min each in transmission mode using Si111 monochromator, collected at the I18 microfocus beamline using Ar purged ion chambers. The XAS normalization and fitting were conducted using the IFEFFIT Demeter software package containing Athena and Artemis, a comprehensive system for processing and analyzing XAS data. The fitting analysis (ARTEMIS) works within FEFF's multiple-scattering path expansion framework, where the data is analyzed as a summation of one or more scattering paths computed by FEFF.[35] For each fitted variable, the value is given with brackets, which denote the standard deviation of the previous figure to indicate the error of the determined value. If no brackets are provided, this indi-

cates that the value has been fixed and is not subject to variability. As the variables in the analysis are not independent, it is necessary to fix certain values to precisely determine other variables. Although some values have been fixed during the fitting process, these values have been determined manually by running fits at different values to find the best fit of the data. Thus, The R-factor is a percentage misfit and a numerical measure of how well the fit overplots the data. For the wavelet transform, k^2-weighted EXAFS spectra were used. The wavelet transforms were done using the code EvAX. A Morlet wavelet mother function was employed for the WT transform of all spectra within the *k*-range of 1–14 $Å^{-1}$. The selection of this wavelet was governed by the fast oscillatory part localized in a Gaussian envelope, making its real and imaginary parts similar to an EXAFS spectrum.[36]

Crystallographic and Defect Simulation: To simulate the XRD and SAED patterns of MoNi alloys, CrystalMaker Software, a powerful tool for understanding the positions of atoms in a three-dimensional (3D) crystal or molecule, was employed. The crystal structure of $MoNi_4$ was modeled by creating unit cells while positioning the atoms in the crystal structure according to the crystal structure provided by ICDD 04-007-0562 reference. In the following, the experimental XRD results were simulated according to the XRD pattern of pristine $MoNi_4$. Meanwhile, lattice plane projection was applied to conduct surface studies to display precise ranges of atoms parallel to specific surface facets. This was done consistently with the experimental XRD results that exhibit preferred orientation in (211) and (310) facets of $MoNi_4$. Further to this step, several simulations were run by varying the following: (i) particulate strain, (ii) unit cell volume contraction/expansion, (iii) preferred orientation, and (iv) Ni metal vacancy concentration.

Electrocatalytic Performance Tests: The electrocatalytic performance was performed with an electrochemical workstation (CHI 760) in a three-electrode cell (50 mL). The Ag/AgCl in 3.5 M KCl was used as a reference electrode, while a graphite plate (2 cm × 2 cm) was used as the counter electrode. As-prepared MoNi electrodes (a mass loading of ≈2 mg cm^{-2} determined by the mass difference) were used as the working electrode. First, the cyclic voltammetry (CV) was scanned for 20 cycles at a scan rate of 50 mV s^{-1} in 1.0 M KOH solution at 25 °C to activate and stabilize the electrode. Then, the LSV was recorded with a scan rate of 5 mV s^{-1}. 85% of iR-compensation was applied to the polarization curves based on the equation: E = E (Ag/AgCl) – iR, where E is the iR-corrected potential, E(Ag/AgCl) is the measured potential with respect to Ag/AgCl in 3.5 M KCl, i is the measured current, and R is the uncompensated resistance (the calculated resistances were in the range of 0.9-2.0 ohm) as determined by electrochemical impedance spectroscopy (EIS). All the potentials in electrochemical measurements were normalized to a reversible hydrogen electrode (RHE) by the equation: E(RHE) = E(Ag/AgCl) + 0.059 pH + 0.205. Overpotential (η) is estimated from the abscissa of the LSV curves for HER in alkaline: η (V) = E – 0.0 V. To eliminate the effect of porosity in Ni foam on the HER activity, electrodes were prepared by drop-casting MoNi powdered catalysts onto a glassy carbon (GC) electrode surface. Specifically, 5 mg of powdered catalyst was mixed with 25 µL of Nafion solution, 475 µL of water, and 500 µL of ethanol. The mixture was sonicated for 30 min to obtain a homogeneous ink. 3 µL of the ink was dropped cast onto the GC electrode (0.07 cm^2) and allowed to dry at room temperature, forming a uniform thin film catalyst layer on the GC. The catalyst-coated GC was used as a working electrode to evaluate the HER activity using the same experimental setup described above. The exchange current densities (j_0, represents the current density at zero overpotential) are calculated using the equation: $j_0 = 10^{-a/b}$, where a is the Tafel intercept and b is the Tafel slope. Faradaic efficiency of hydrogen production was evaluated by quantifying the reaction products by online gas chromatography equipped with a thermal conductivity detector. The stability tests were carried out by chronopotentiometry at 1000 mA cm^{-2}, and at different current densities in the range of 50–400 mA cm^{-2}. The dynamic specific resistance variation was tested using EIS at a potential of −0.1 V versus RHE and frequency of 10000 Hz, and Bond-phase plots at a potential of −0.1 V versus RHE and frequency range of 0.1–100000 Hz. The semi-logarithmic plot of the inverse charge-transfer resistance, R_{ct}^{-1}, was conducted at potentials of −0.050, −0.075, −0.100, and −0.125 V versus RHE.

Density Functional Theory Calculations: All theoretical simulations were performed using ab initio total energy calculations based on DFT within VASP framework (Vienna Ab initio Simulation Packages) code, with a plane wave basis set for the electronic orbitals. The electronic exchange and correlation were described within the generalized gradient approximation using the Perdew-Burke-Ernzerhof (PBE) functional. The interaction of the valence electrons with the ionic cores was treated using the projector augmented-wave (PAW) method.[37] A Monkhorst-Pack grid was used by K-points 5 × 5 × 1. The employed cut-off energy was set as 450 eV. An electronic smearing was introduced within the Methfessel-Paxton scheme with N = 0 and σ = 0.1 eV.[38] Spin-polarization effect was considered for MoNi alloy surfaces. According to the XRD results, perfect and defective $MoNi_4$ (312), (310), and (211) surfaces are modeled. All DFT calculations were performed to minimize all the residual forces until the convergence criterion of 0.01 eV $Å^{-1}$. The central difference was used to calculate the zero-point energy (ZPE). Considering the contributions from zero-point energy and entropy, the adsorption-free energy of hydrogen species is given by Equation (1):

$$\Delta G\,(H^*) = \Delta E + \Delta ZPE - T\Delta S \quad (1)$$

The value of TΔS at 298 K is adapted. Thus, referring to H_2 (gas) free energy, the binding energy Δ*E* is given by Equation (2):

$$\Delta E = E\,(H/slab) - E\,(slab) - 0.5 \times E\,(H_2) \quad (2)$$

where E(H/slab) and E(slab) are the total energies of hydrogen species adsorption on the slab and the clean slab.

Supporting Information

Supporting Information is available from the Wiley Online Library or from the author.

Acknowledgements

The study is supported by the Australian Renewable Energy Agency (ARENA) and the Australian Research Council (IC200100023, DP220103294, and CE230100017). Y.W. acknowledges the International Hydrogen Research Fellowship Program financially supported by CSIRO, DCCEEW, the Australian Hydrogen Research Network (AHRN) and the Australian Research Council (DE230100327 and LP220200583). H. A. acknowledges the support from the DCCEEW International Clean Innovation Researcher Networks Grant (ICIRN000011). Distinguished Professor Suresh Bhargava expresses his gratitude toward his mentor and PhD supervisor the late Professor E. W. Abel, University of Exeter (UK), for giving him the power of knowledge and mentorship to produce the next generation of scientists. The authors acknowledge the Australian Synchrotron and Diamond Light Source in the UK. Special thanks are extended to Dr Magnus Garbrecht for his assistance in HRTEM analysis and access to the electron microscopy facilities of Sydney Microscopy and Microanalysis at the University of Sydney. The authors thank Drs Edwin Mayes, Matthew Field, and Billy Murdoch from the RMIT Microscopy and Microanalysis Facility (RMMF) for their assistance with the TEM, SEM, and XPS analyses.

Open access publishing facilitated by The University of Melbourne, as part of the Wiley - The University of Melbourne agreement via the Council of Australian University Librarians.

Conflict of Interest

Y. Wang, H. Arandiyan, and C. Zhao filed an International (PCT) Patent Application (No. PCT/AU2023/05 1138) based on the work reported in this paper.

Author Contributions

Y.W. carried out Investigation, Methodology, Resources, Formal analysis, Writing – original draft, and Writing – review & editing. H.A. conducted Conceptualization, Investigation, Resources, Methodology, Writing – original draft, and Writing – review & editing. S.S.M. dealt with Investigation, Formal analysis, Writing – original draft, and Writing – review & editing. X.S. conducted Methodology, Investigation, and Formal analysis. S.A.B. dealt with Methodology, Investigation, and Formal analysis. P.K. conducted Methodology and Formal analysis. C.C.S. dealt with Methodology, Formal analysis, Writing – original draft, and Writing – review & editing. H.S. dealt with Methodology, Investigation, and Formal analysis. C. P. carried out Writing – review & editing. K.D. dealt with Conceptualization, Methodology, and Writing – review & editing. S.B. carried out Methodology, Investigation, and Formal analysis. S.K.B. conducted Conceptualization and methodology. C.Z. carried out Conceptualization, Supervision, Methodology, Investigation, Resources, Funding acquisition, and Writing – review & editing. Y.W., H.A., and C.Z. coordinated the cooperation of all co-authors and generated the final draft. All authors contributed to the draft revisions.

Data Availability Statement

The data that support the findings of this study are available in the supporting information of this article.

Keywords

defect, high current density, hydrogen evolution reaction, MoNi alloy, stacking fault

Received: February 8, 2024
Revised: June 1, 2024
Published online: June 23, 2024

[1] a) J. B. Zimmerman, P. T. Anastas, H. C. Erythropel, W. Leitner, *Science* **2020**, *367*, 397; b) C. Rong, X. Shen, Y. Wang, L. Thomsen, T. Zhao, Y. Li, X. Lu, R. Amal, C. Zhao, *Adv. Mater.* **2022**, *34*, 2110103; c) C. Qiu, S. He, Y. Wang, Q. Wang, C. Zhao, *Chem. Eur. J.* **2020**, *26*, 4120.

[2] C. Hu, L. Zhang, J. Gong, *Energy Environ. Sci.* **2019**, *12*, 2620.

[3] a) D. Zhang, H. Li, A. Riaz, A. Sharma, W. Liang, Y. Wang, H. Chen, K. Vora, D. Yan, Z. Su, A. Tricoli, C. Zhao, F. J. Beck, K. Reuter, K. Catchpole, S. Karuturi, *Energy Environ. Sci.* **2022**, *15*, 185; b) L. Xie, L. Wang, W. Zhao, S. Liu, W. Huang, Q. Zhao, *Nat. Commun.* **2021**, *12*, 5070; c) L. Xie, L. Wang, X. Liu, W. Zhao, S. Liu, X. Huang, Q. Zhao, *Angew. Chem., Int. Ed.* **2024**, *63*, 202316306; d) B. Li, K. Nie, Y. Zhang, L. Yi, Y. Yuan, S. Chong, Z. Liu, W. Huang, *Adv. Mater.* **2023**, *35*, 2303285.

[4] J. Zhu, L. Hu, P. Zhao, L. Y. S. Lee, K.-Y. Wong, *Chem. Rev.* **2020**, *120*, 851.

[5] T. Zhao, Y. Wang, X. Chen, Y. Li, Z. Su, C. Zhao, *ACS Sustainable Chem. Eng.* **2020**, *8*, 4863.

[6] H. Arandiyan, S. S. Mofarah, Y. Wang, C. Cazorla, D. Jampaiah, M. Garbrecht, K. Wilson, A. F. Lee, C. Zhao, T. Maschmeyer, *Chem. Eur. J.* **2021**, *27*, 14418.

[7] a) F. Calle-Vallejo, J. Tymoczko, V. Colic, Q. H. Vu, M. D. Pohl, K. Morgenstern, D. Loffreda, P. Sautet, W. Schuhmann, A. S. Bandarenka, *Science* **2015**, *350*, 185; b) Z. Zhang, G. Liu, X. Cui, Y. Gong, D. Yi, Q. Zhang, C. Zhu, F. Saleem, B. Chen, Z. Lai, Q. Yun, H. Cheng, Z. Huang, Y. Peng, Z. Fan, B. Li, W. Dai, W. Chen, Y. Du, L. Ma, C.-J. Sun, I. Hwang, S. Chen, L. Song, F. Ding, L. Gu, Y. Zhu, H. Zhang, *Sci. Adv.* **2021**, *7*, eabd6647; c) J. Zhang, T. Wang, P. Liu, Z. Liao, S. Liu, X. Zhuang, M. Chen, E. Zschech, X. Feng, *Nat. Commun.* **2017**, *8*, 15437; d) J. D. Butson, A. Sharma, H. Chen, Y. Wang, Y. Lee, P. Varadhan, M. N. Tsampas, C. Zhao, A. Tricoli, H. H. Tan, C. Jagadish, S. Karuturi, *Adv. Energy Mater.* **2022**, *12*, 2102752.

[8] Y. Xu, J. Yang, T. Liao, R. Ge, Y. Liu, J. Zhang, Y. Li, M. Zhu, S. Li, W. Li, *Chem. Eng. J.* **2022**, *431*, 134126.

[9] a) R. Jiang, Y. Da, J. Zhang, H. Wu, B. Fan, J. Li, J. Wang, Y. Deng, X. Han, W. Hu, *Appl. Catal., B* **2022**, *316*, 121682; b) Z. Li, J.-Y. Fu, Y. Feng, C.-K. Dong, H. Liu, X.-W. Du, *Nat. Catal.* **2019**, *2*, 1107.

[10] a) H. Arandiyan, S. S. Mofarah, C. C. Sorrell, E. Doustkhah, B. Sajjadi, D. Hao, Y. Wang, H. Sun, B.-J. Ni, M. Rezaei, Z. Shao, T. Maschmeyer, *Chem. Soc. Rev.* **2021**, *50*, 10116; b) M. Ohring, in *Materials Science of Thin Films (Second Edition)* (Ed: M. Ohring), Academic Press, San Diego **2002**.

[11] a) H. Liu, M. Jin, D. Zhan, J. Wang, X. Cai, Y. Qiu, L. Lai, *Appl. Catal., B* **2020**, *272*, 118951; b) J. Hwang, Z. Feng, N. Charles, X. R. Wang, D. Lee, K. A. Stoerzinger, S. Muy, R. R. Rao, D. Lee, R. Jacobs, D. Morgan, Y. Shao-Horn, *Mater. Today* **2019**, *31*, 100.

[12] a) Y. Wang, H. Arandiyan, X. Chen, T. Zhao, X. Bo, Z. Su, C. Zhao, *J. Phys. Chem. C* **2020**, *124*, 9971; b) Y. Wang, T. Wang, H. Arandiyan, G. Song, H. Sun, Y. Sabri, C. Zhao, Z. Shao, S. Kawi, *Adv. Mater.* **2024**, *36*, 2313378.

[13] I. Kovács, H. El Sayed, *J. Mater. Sci.* **1976**, *11*, 529.

[14] a) P. Liu, L.-c. Liu, H.-r. Gong, *J. Cent. South Univ.* **2021**, *28*, 39; b) K. Edalati, Z. Horita, *Acta Mater.* **2011**, *59*, 6831.

[15] D. Jampaiah, V. K. Velisoju, D. Devaiah, M. Singh, E. L. H. Mayes, V. E. Coyle, B. M. Reddy, V. Bansal, S. K. Bhargava, *Appl. Surf. Sci.* **2019**, *473*, 209.

[16] Y. Suzuki, Y. Hattori, J. Nozawa, S. Uda, A. Toyotama, J. Yamanaka, *Crystals* **2016**, *6*, 80.

[17] B. Hammer, J. K. Nørskov, *Adv. Catal.* **2000**, *45*, 71.

[18] Y. Yang, Y. Qian, Z. Luo, H. Li, L. Chen, X. Cao, S. Wei, B. Zhou, Z. Zhang, S. Chen, W. Yan, J. Dong, L. Song, W. Zhang, R. Feng, J. Zhou, K. Du, X. Li, X.-M. Zhang, X. Fan, *Nat. Commun.* **2022**, *13*, 7225.

[19] Y. Duan, Z.-Y. Yu, L. Yang, L.-R. Zheng, C.-T. Zhang, X.-T. Yang, F.-Y. Gao, X.-L. Zhang, X. Yu, R. Liu, H.-H. Ding, C. Gu, X.-S. Zheng, L. Shi, J. Jiang, J.-F. Zhu, M.-R. Gao, S.-H. Yu, *Nat. Commun.* **2020**, *11*, 4789.

[20] a) M. Wang, H. Yang, J. Shi, Y. Chen, Y. Zhou, L. Wang, S. Di, X. Zhao, J. Zhong, T. Cheng, W. Zhou, Y. Li, *Angew. Chem., Int. Ed.* **2021**, *60*, 5771; b) J. Mao, W. Chen, D. He, J. Wan, J. Pei, J. Dong, Y. Wang, P. An, Z. Jin, W. Xing, H. Tang, Z. Zhuang, X. Liang, Y. Huang, G. Zhou, L. Wang, D. Wang, Y. Li, *Sci. Adv.* **2017**, *3*, 1603068.

[21] R. D. Shannon, *Acta Cryst.* **1976**, *A32*, 751.

[22] D. S. Aidhy, C. Lu, K. Jin, H. Bei, Y. Zhang, L. Wang, W. J. Weber, *Scr. Mater.* **2016**, *114*, 137.

[23] E. Asadi, M. A. Zaeem, A. Moitra, M. A. Tschopp, *J. Phys.: Condens. Matter* **2014**, *26*, 115404.

[24] a) H. Xu, B. J. Wiley, *Chem. Mater.* **2021**, *33*, 8301; b) V. Germain, J. Li, D. Ingert, Z. L. Wang, M. P. Pileni, *J. Phys. Chem. B* **2003**, *107*, 8717.

[25] a) T. Shinagawa, A. T. Garcia-Esparza, K. Takanabe, *Sci. Rep.* **2015**, *5*, 13801; b) A. Laszczyńska, I. Szczygieł, *Int. J. Hydrogen Energy* **2020**, *45*, 508.

[26] W. F. Chen, C. H. Wang, K. Sasaki, N. Marinkovic, W. Xu, J. T. Muckerman, Y. Zhu, R. R. Adzic, *Energy Environ. Sci.* **2013**, *6*, 943.

[27] a) Z. Zheng, L. Yu, M. Gao, X. Chen, W. Zhou, C. Ma, L. Wu, J. Zhu, X. Meng, J. Hu, Y. Tu, S. Wu, J. Mao, Z. Tian, D. Deng, *Nat. Commun.* **2020**, *11*, 3315; b) X. Zheng, Y. Chen, X. Bao, S. Mao, R. Fan, Y. Wang, *ACS Catal.* **2020**, *10*, 11634; c) S. Jiang, R. Zhang, H. Liu, Y. Rao, Y. Yu, S. Chen, Q. Yue, Y. Zhang, Y. Kang, *J. Am. Chem. Soc.* **2020**, *142*, 6461; d) Y. Wang, A. Sharma, T. Duong, H. Arandiyan, T. Zhao, D. Zhang, Z. Su, M. Garbrecht, F. J. Beck, S. Karuturi, C. Zhao, K. Catchpole, *Adv. Energy Mater.* **2021**, *11*, 2101053.

[28] K. Dastafkan, S. Wang, C. Rong, Q. Meyer, Y. Li, Q. Zhang, C. Zhao, *Adv. Funct. Mater.* **2022**, *32*, 2107342.
[29] J. K. Nørskov, T. Bligaard, A. Logadottir, J. R. Kitchin, J. G. Chen, S. Pandelov, U. Stimming, *J. Electrochem. Soc.* **2005**, *152*, J23.
[30] G. Yuan, J. Bai, B. Gao, L. Ren, J. Mei, L. Zhang, *Inorg. Chem. Commun.* **2020**, *111*, 107595.
[31] H. Yang, Z. Chen, P. Guo, B. Fei, R. Wu, *Appl. Catal., B* **2020**, *261*, 118240.
[32] X. Zou, Y. Wu, Y. Liu, D. Liu, W. Li, L. Gu, H. Liu, P. Wang, L. Sun, Y. Zhang, *Chem* **2018**, *4*, 1139.
[33] H. Liu, C. Xi, J. Xin, G. Zhang, S. Zhang, Z. Zhang, Q. Huang, J. Li, H. Liu, J. Kang, *Chem. Eng. J.* **2021**, *404*, 126530.
[34] Y. Jing, H. Liu, R. Yan, J. Chen, H. Dai, C. Liu, X.-D. Zhang, *ACS Appl. Nano Mater.* **2019**, *2*, 5922.
[35] B. Ravel, M. Newville, *J. Synchrotron Rad.* **2005**, *12*, 537.
[36] J. Timoshenko, A. Kuzmin, J. Purans, *J. Phys.: Condens. Matter* **2014**, *26*, 055401.
[37] P. E. Blöchl, *Phys. Rev. B* **1994**, *50*, 17953.
[38] M. Methfessel, A. T. Paxton, *Phys. Rev. B* **1989**, *40*, 3616.